Chinese Chemical Letters 37 (2026) 111328

Contents lists available at ScienceDirect

Chinese Chemical Letters

journal homepage: www.elsevier.com/locate/cclet

# MOF derived Pt-$In_2O_3$ hollow microtube for ultrasensitive ppb-level detection of *p*-xylene and aging characteristics analysis

Huanhuan Zhang[a,1], Shisong Guo[a,1], Yanxiang Chen[a,1], Yan Bai[a], Shuyang Ye[a], Sha Zhang[a], Xinyi Chen[a], Peng Wang[a], Anqi Li[b], Long Li[d], Bingbing Chen[e], Hua-Yao Li[a,b,c,d,*], Huan Liu[a]

[a] School of Integrated Circuits, Huazhong University of Science and Technology, Wuhan 430074, China
[b] School of Future Technology, Huazhong University of Science and Technology, Wuhan 430074, China
[c] Shenzhen Huazhong University of Science and Technology Research Institute, Shenzhen 518057, China
[d] Wenzhou Advanced Manufacturing Institute, Huazhong University of Science and Technology, Wenzhou 325000, China
[e] School of Energy Science and Engineering, Nanjing Tech University, Nanjing 211816, China

ARTICLE INFO

*Article history:*
Received 1 March 2025
Revised 30 April 2025
Accepted 15 May 2025
Available online 17 May 2025

*Keywords:*
Metal-organic framework
Pt-$In_2O_3$ microtube
*p*-Xylene detection
Stability
Aging mechanism

ABSTRACT

Metal-organic framework (MOF) derived metal oxides and their composites have shown remarkable potential in enhancing the sensitivity and lowering the detection limits of gas sensors, emerging as promising candidates for volatile organic compound (VOC) detection. Here, the Pt-sensitized $In_2O_3$ hollow microtubes were synthesized from MIL-68 *via* hydrothermal and sacrificial template methods, demonstrating exceptional trace detection capability (0.01–1 ppm) to *p*-xylene. The 2% Pt NPs-$In_2O_3$ showed the highest response of 68.7 at 50 ppb, with a theoretical detection limit as low as 0.027 ppb. The role of Pt was elucidated through comprehensive characterization, revealing that highly dispersed Pt nanoparticles form a well-defined interface with $In_2O_3$, enhancing gas adsorption, electron transfer, and reaction kinetics, thereby significantly boosting sensor performance. By integrating *in situ* diffuse reflectance infrared Fourier transform spectroscopy (DRIFTS), this study provides fundamental insights into gas-solid interfacial sensing mechanisms, elucidating how Pt modulation enhances gas sensor performance at the molecular level. Additionally, the aging mechanisms of 2% Pt NPs-$In_2O_3$ sensors were explored through *in situ* characterization, revealing the evolution of surface morphology and gas adsorption capacity before and after aging under different conditions: 200 °C/0% RH, 200 °C/50% RH, and 250 °C/0% RH for 20 days. These findings offer valuable guidance for improving the long-term stability and reliability of Pt-modified $In_2O_3$ gas sensors.

© 2026 Published by Elsevier B.V. on behalf of Chinese Chemical Society and Institute of Materia Medica, Chinese Academy of Medical Sciences.

Xylene is a typical volatile organic compounds (VOCs) commonly found in daily life, originating from sources such as furniture decoration, ink printing, and industrial manufacturing [1,2]. As a toxic, colorless, and sweet-smelling VOC, xylene poses significant risks to human health. Prolonged exposure can lead to respiratory diseases, neurasthenia syndrome, and is associated with an increased risk of leukemia [3–5]. Xylene exists in three isomeric forms, *ortho*-, *meta*-, and *para*-xylene, which share the same chemical formula but differ in molecular structure. Among them, *p*-xylene has the most extensive industrial applications, primarily serving as a key precursor in polyester production, and is one of the most prevalent indoor air pollutants [6]. Given its widespread presence and potential health hazards, the development of fast and accurate *p*-xylene monitoring technologies is essential to safeguarding public health.

Semiconductor metal oxides (SMOs) based sensors are particularly notable for their high chemical stability, simple structure, and ease of fabrication [7]. A wide variety of semiconductor materials, such as $SnO_2$ [8], ZnO [9], $WO_3$ [10] and $In_2O_3$ [11] have been explored as sensing materials for VOCs detection. However, issues such as low sensitivity, high power consumption, and poor selectivity continue to hinder the performance of conventional SMOs in VOCs sensing applications. To address these challenges, the rational design of mesoporous and hollow hierarchical structures with high active sites [12], construction of heterojunctions [13], heteroatom doping [14] and noble-metal modifications, can significantly enhance sensing performance[15]. Among various methods, incorporating noble metals has been demonstrated to effectively enhance sensing performance, a result of the synergistic effects from both chemical and electronic sensitization [16]. Noble metal nanoparti-

* Corresponding author.
*E-mail address:* huayaoli@hust.edu.cn (H.-Y. Li).
[1] These authors contributed equally to this work.

https://doi.org/10.1016/j.cclet.2025.111328
1001-8417/© 2026 Published by Elsevier B.V. on behalf of Chinese Chemical Society and Institute of Materia Medica, Chinese Academy of Medical Sciences.

cles deposited on metal oxides act as catalysts, facilitating the interaction between the target gas and the sensing interface, speeding up the adsorption and desorption of gas molecules. Additionally, these catalysts may act as electron donors or acceptors, influencing the carrier concentration and energy levels of the SMOs, thereby enabling efficient charge transfer [17]. However, the free noble-metal NPs have high surface energies and tend to aggregate degrading sensor performance and compromise long-term reliability [18]. Thus, the development of a new strategy to stabilize NPs is necessary to address practical and commercial consideration.

Recently, the metal-organic frameworks (MOFs) have garnered increasing interest from researchers as novel templates characterized by its tailored structures, high porosity, and customizable functionalities which are extensively used in the gas sensors field [12,19]. The annealed MOF material exhibited remarkable advantages toward application in gas sensors owing to its high porosity and chemical tunability originating from MOF precursors [20]. According to the reports, the MIL-68(In) derived $In_2O_3$ nanomaterials can inherit the porous cavity nanorods structure of the precursor, which helps the gas diffusion and provide more adsorption sites [21]. Sun *et al.* [22] have studied the In-MIL(68) derived $In_2O_3$ materials for triethylamine sensing and the sensor showed a high response for 5 ppm target gas. Liu *et al.* [23] prepared $In_2O_3$/ZnO using the MIL-68/ZIF-8 sacrificial template and achieved a response of 44.6 to triethylamine (100 ppm) at 100 °C, which exhibits the great potential for VOCs detection applications. Additionally, MIL-68(In) serves as promising platforms for loading ultrasmall noble metal nanoparticles due to their high porosity and cavity structure, which effectively prevent the growth and aggregation of noble metal nanoparticles (NPs) [24,25]. Noble metal-loaded MIL-68(In) can be easily transformed to mesoporous SMOs functionalized by uniformly dispersed noble catalysts, which are highly effective to enhance the sensing performance through the catalytic reaction, chemical/electronic sensitization effects and formation of heterojunctions. However, the gas-solid reaction mechanisms and the aging behavior of noble metal-loaded MIL-68(In) derivative-based gas sensors have rarely been studied in detail.

In this work, we presented a MOFs-derived Pt nanoparticle loaded $In_2O_3$ hollow microtube (Pt NPs/$In_2O_3$) based on MIL-68(In) template. The MOF derived $In_2O_3$ was prepared *via* hydrothermal method followed by calcination, and then its properties were regulated by Pt cation impregnation strategy. The 2 % Pt NPs-$In_2O_3$ demonstrated an ultrasensitive response to *p*-xylene gas ($R_a/R_g$= 68.7 at 50 ppb), low theoretical detection limit (0.027 ppb), and excellent selectivity towards other interfering gases at optimal operating temperature. For practical applications, long-term variations in resistance and response directly affect sensing precision and accuracy. To address this, we conducted a 20-day laboratory aging test and performed *in situ* characterization to gain deeper insights into the mechanisms driving the gas-sensing aging process.

Fig. 1a illustrates the comprehensive fabrication process of the gas sensor, which begins with the hydrothermal synthesis of the MIL-68 framework, followed by the incorporation of Pt nanoparticles into MIL-68-derived $In_2O_3$ to fabricate a *p*-xylene-sensitive material. The synthesized $In_2O_3$ exhibits a well-defined microtubular morphology with a uniform size distribution (Figs. 1b and c). The microtubes possess a hollow structure with a distinct hexagonal cross-section, exhibiting an average length of approximately 10–20 μm and a diameter ranging from 500 nm to 1000 nm (Fig. 1c). Figs. 1d and e show the TEM image of the 2 % Pt NPs-$In_2O_3$ composite, which retains the hollow tubular structure of pure $In_2O_3$, indicating that the incorporation of Pt nanoparticles does not significantly affect the overall morphology [26]. The tube walls, composed of nanoparticles 10–20 nm in diameter, exhibit a loose, porous structure, providing abundant active sites for gas adsorption [27]. The HRTEM image of the interface (Fig. 1f) reveals well-

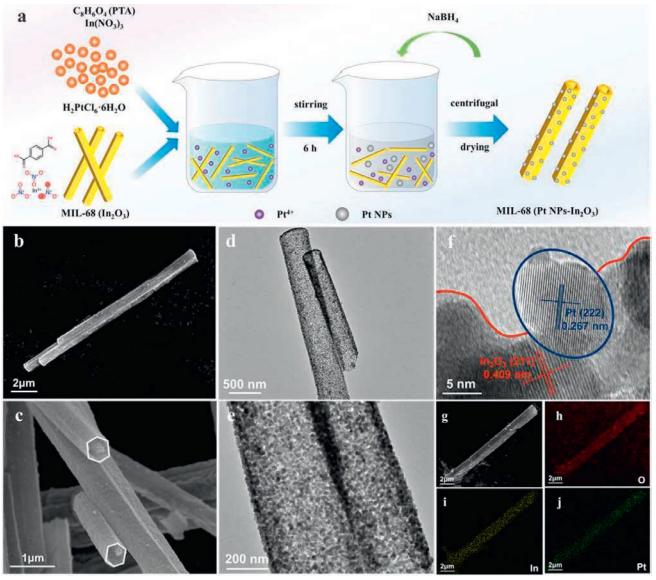



**Fig. 1.** (a) Schematic diagram of the synthesis process of Pt loaded MIL-68 ($In_2O_3$) semiconductor gas sensitive material. (b, c) SEM images of MIL-68($In_2O_3$). (d, e) TEM image of MIL-68(2 % Pt NPs-$In_2O_3$). (f) HRTEM image of MIL-68(2 % Pt NPs-$In_2O_3$). (g) SEM image of MIL-68(2 % Pt NPs-$In_2O_3$) and its corresponding element mapping images, (h) O element, (i) In element and (j) Pt element.

defined lattice fringes with spacings of 0.409 nm and 0.267 nm, corresponding to the (211) plane of $In_2O_3$ and the (222) plane of Pt NPs, respectively. A distinct interface between the Pt NPs and the $In_2O_3$ matrix is observed, indicating a relatively compact bonding state. The SEM image of MIL-68(2 % Pt NPs-$In_2O_3$) (Fig. 1g) and corresponding elemental mapping results (Figs. 1h-j) confirm the presence of In, O, and Pt elements, showing a uniform distribution of Pt NPs within the $In_2O_3$ tubular matrix.

The XRD patterns of as prepared samples are shown in Fig. 2a. The diffraction peaks of all samples match well with the $In_2O_3$ standard PDF card (JCPDS No. 71–2194) [28]. The sharp diffraction peaks and absence of impurity peaks confirm the high crystallinity and purity of the prepared samples. Notably, no distinct Pt phase diffraction peaks appear in the XRD patterns of Pt NPs, likely due to the low loading and high dispersion of Pt NPs. The average crystalline sizes of pure $In_2O_3$, 2 % Pt NPs-$In_2O_3$, 4 % Pt NPs-$In_2O_3$, and 6 % Pt NPs-$In_2O_3$ were calculated using the Debye-Scherrer equation [29], yielding values of 13.5, 12.3, 12.6, and 12.7 nm, respectively. The incorporation of a noble metal phase (Pt) modulates the surface chemistry of $In_2O_3$, thereby altering its crystallization kinetics, affecting both nucleation and grain growth rates [30,31]. Fourier-transform infrared (FT-IR) spectroscopy was conducted to confirm the chemical composition of pure $In_2O_3$ and Pt NPs-$In_2O_3$. The characteristic peaks at 417, 539, 566, and 601 $cm^{-1}$ correspond to the vibrational modes of $In_2O_3$ (Fig. 2b) [32,33]. The intensity of the In-O vibration peaks remains stable with increasing Pt loading, confirming Pt exists in its elemental form without disrupting the In-O bonding structure [32].

The BET method was used to analyze the internal and surface structure of $In_2O_3$ and Pt NPs-$In_2O_3$ samples (Fig. 2c). The $N_2$ adsorption-desorption isotherms of all samples exhibit a typical type-IV curve, with adsorption behavior at low relative pressure ($P/P_n$ < 0.01), indicating the presence of micropores [34,35]. The BET specific surface areas of pure $In_2O_3$, 2 % Pt NPs-$In_2O_3$, 4 % Pt NPs-$In_2O_3$, and 6 % Pt NPs-$In_2O_3$ were 49.33, 86.21, 70.69, and 74.76 $m^2/g$, respectively, demonstrating a significant increase upon Pt incorporation. This conclusion is further substantiated by the pore size distribution depicted in Fig. 2d, where the pores in all

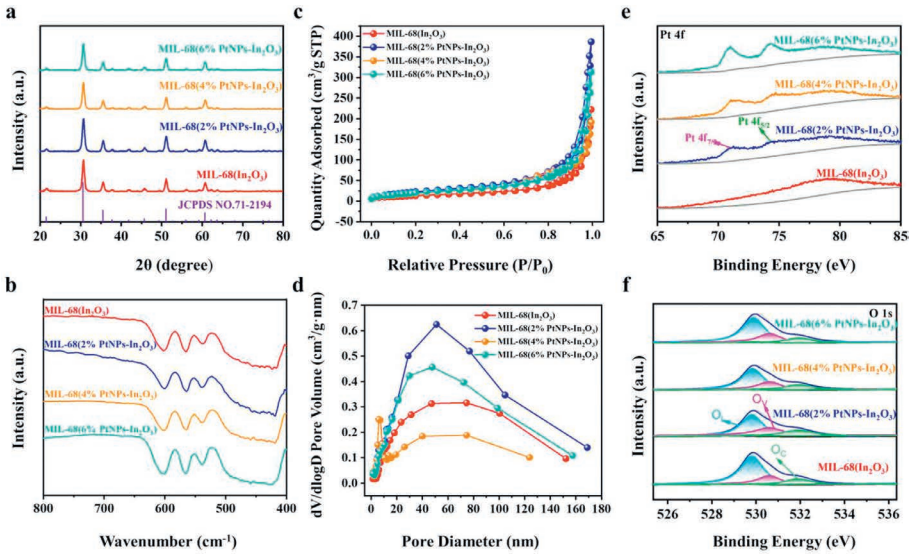



**Fig. 2.** (a) XRD diffraction patterns of MIL-68 precursor, pure $In_2O_3$ sample and Pt NPs-$In_2O_3$ samples with different ratios. (b) FT-IR spectra of pure $In_2O_3$ sample and Pt NPs-$In_2O_3$ samples with different ratios. (c) Nitrogen adsorption-desorption isotherms and (d) pore size distribution curves of pure $In_2O_3$ sample and Pt NPs-$In_2O_3$ samples with different ratios. (e) Pt 4f XPS spectra and (f) O 1s XPS spectra of pure $In_2O_3$ sample and Pt NPs-$In_2O_3$ samples with different ratios.

four samples are predominantly mesoporous, with diameters ranging from 20 nm to 50 nm, and additionally include some macropores within the 50–100 nm range. These advantages features can provide reaction sites and diffusion channels for gas molecules, thereby enhancing the performance of gas sensing.

The chemical states of Pt and O in all four samples were analyzed to clarify the surface oxygen vacancy density changes in Figs. 2e and f. All binding energies (BE) are referenced to the C 1s peak at 284.6 eV. The peaks at 71.0 and 74.3 eV correspond to Pt $4f_{7/2}$ and Pt $4f_{5/2}$ in the 4f orbit, indicating Pt exists solely in the zero-valence state (Fig. 2e) [36,37]. The high-resolution XPS O 1s spectra of the four samples (Fig. 2f) reveal three distinct oxygen species. The peaks at 529.8, 530.6, and 532.0 eV correspond to lattice oxygen ($O_L$), oxygen species adsorbed on vacancies ($O_V$), and chemisorbed oxygen species ($O_C$), respectively [34,38,39]. The area ratios of these oxygen species are detailed in Table S1 (Supporting information). Notably, the amounts of $O_C$ with Pt-doping are much higher than those of pristine $In_2O_3$ and the $O_C$ ratio initially increases and then decreases with rising Pt content, peaking at 2%. This phenomenon can be attributed to the "spillover effect" of Pt, which can induce the adsorption and desorption of molecular oxygen on the surface of $In_2O_3$ [40]. The $O_C$ of 2% Pt NPs-$In_2O_3$ is higher than that on 4%/6% Pt NPs-$In_2O_3$, indicating that the appropriate addition of smaller Pt nanoparticles in 2% Pt NPs-$In_2O_3$ leads to a greater formation of surface-adsorbed oxygen. In contrast, excessive Pt content weakens the Pt-$In_2O_3$ interaction, reducing the ability to adsorb and activate oxygen [41].

The gas sensing performance of $In_2O_3$ and Pt NPs-$In_2O_3$ was evaluated using a dynamic measurement system and alumina substrate devices with gold electrodes. To assess the impact of operating temperature on sensor performance, the dependence of the sensor response to *p*-xylene at a concentration of 10 ppm was investigated. Compared with the pure $In_2O_3$ without Pt loading, the *p*-xylene gas sensing performance of all Pt NPs-$In_2O_3$ composites improved, and exhibited a "volcano" trend with work temperature increasing from 65 °C to 315 °C. Compared to the $In_2O_3$ sensors, the optimal operating temperature for Pt NPs-$In_2O_3$ sensors decreased to 200 °C. To detect *p*-xylene at ppb levels, the sensors were tested across a concentration range of 50–1000 ppb at 200 °C. The dynamic response curves for the four sensors are shown in Fig. 3b. The sensors displayed a strong response when exposed to *p*-xylene, which then gradually decreased and stabilized in air. With increasing Pt content, the response initially increases and then declines. Wherein, the improvement in gas sensing properties can be explained by the loaded Pt particles exerting the catalytic spillover effect they possess, leading to an increase in response. Of these, the 2% Pt NPs-$In_2O_3$ gas sensor achieves the best sensing performance, with the response of 214.63 for 1000 ppb *p*-xylene. The response time of all sensor samples shows the same trend (Fig. S2 in Supporting information), decreasing with increasing *p*-xylene concentration, but Pt NPs-$In_2O_3$ sensor gas sensors show the faster response compared with the pristine $In_2O_3$. This phenomenon is attributed to the deposition of Pt on the metal oxide, which acts as a catalyst, promoting the interaction between the target gas and the sensing interface, thereby accelerating the adsorption of gas molecules [17]. Moreover, the sensors successfully detected *p*-xylene at 10 ppb, demonstrating performance comparable to *p*-xylene sensors reported in previous studies (Table S2 in Supporting information). According to the definition of the International Union of Pure and Applied Chemistry (IUPAC), the theoretical lower detection limit (LOD) of the sensor was calculated by linear fitting and three-sigma method. The calculation formula is as follows [42,43]:

$$\mathrm{LOD(ppb)} = \frac{3RMS_{\mathrm{noise}}}{\mathrm{Slope}} \quad (1)$$

where $RMS_{\mathrm{noise}}$ is the noise of the sensor in the baseline phase, *Slope* is the slope of the linear region of the sensor response-gas concentration function curve. As shown in Fig. S1 (Supporting information), the LOD of the 2% Pt NPs-$In_2O_3$ sensor is 0.027 ppb, compared to 3.00 ppb for the pure $In_2O_3$ sensor.

To assess the practical application of the sensors, their anti-interference performance and stability under varying environmental conditions were evaluated. In a humid environment, sensor performance is affected by competition between water and gas molecules, leading to a reduced response [43]. The response decreases as relative humidity (RH) rises from 10% to 70% (Fig. 3d). However, the 2% Pt NPs-$In_2O_3$ sensor still delivers a significant response to 500 ppb *p*-xylene, much higher than the pure $In_2O_3$ sensor. To underscore its potential for high-performance sensing in practical settings, the reproducibility and long-term stability of the sensors at the optimal operating temperature were evaluated. The 2% Pt NPs-$In_2O_3$ sensor exhibited consistent responses with

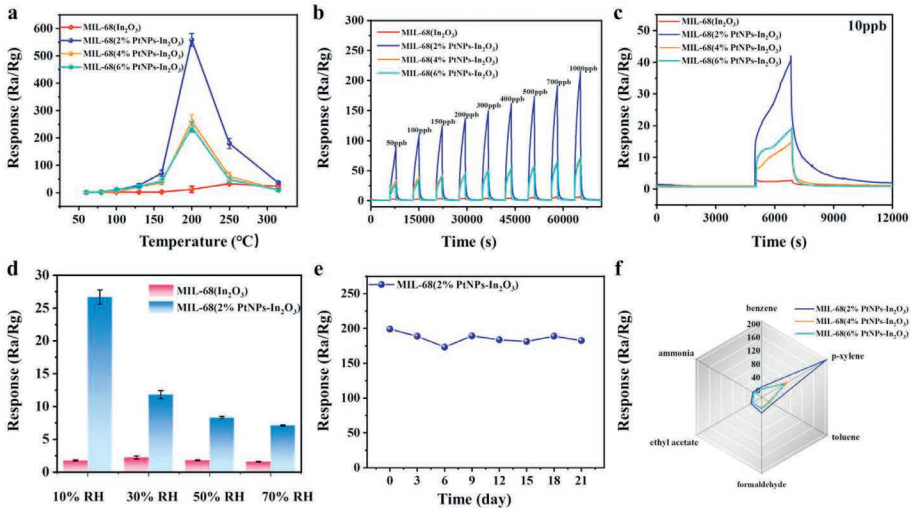



**Fig. 3.** (a) Response of gas sensors based on $In_2O_3$ and Pt NPs-$In_2O_3$ to 10 ppm *p*-xylene gas at different operating temperatures. (b) Dynamic response curves of four gas sensors for testing 50–1000 ppb *p*-xylene at 200 °C. (c) Dynamic response curves of four gas sensors to 10 ppb *p*-xylene gas at 200 °C. (d) Response of pure $In_2O_3$ sensor and 2 % Pt NPs-$In_2O_3$ sensor toward 500 ppb *p*-xylene at different relative humidity at 200 °C. (e) Long-term stability tests of 2 % Pt NPs-$In_2O_3$ sensor to 1000 ppb *p*-xylene at 200 °C. (f) Response of the sensors toward diverse target gases at concentration of 1000 ppb at 200 °C.

minimal deviation over five cycles at 10 ppb *p*-xylene (Fig. S3 in Supporting information). When exposed to 1000 ppb *p*-xylene at 200 °C for 30 days (Fig. 3e), the sensor maintained its response without significant decay. Overall, the 2 % Pt NPs-$In_2O_3$ sensor demonstrates the potential for ppb-level *p*-xylene detection, underscoring its promising application in gas sensing. The selectivity of the pure $In_2O_3$ sensor and Pt NPs-$In_2O_3$ sensors was evaluated at 200 °C for 1000 ppb of several potential interfering gases, including benzene, toluene, formaldehyde, ethyl acetate, and ammonia. As shown in Fig. 3f and Fig. S4 (Supporting information), all the sensors exhibited the highest response to *p*-xylene. Notably, the 2 % Pt NPs-$In_2O_3$ sensor demonstrated superior selectivity for *p*-xylene detection.

The widely accepted sensing mechanism of semiconductor gas sensors depends on the resistance variation of the sensing material, which involves the adsorption of surface oxygen species and the oxidation–reduction reaction between oxygen species and target gas molecules [7,44–46]. In this work, both pure $In_2O_3$ sensor and 2 % Pt NPs-$In_2O_3$ sensor exhibit n-type semiconductor sensing behavior. In the atmospheric environment, the oxygen molecules adsorbed on the surface of sensing layer can capture electrons from the conduction band to form active oxygen species, which leads to the formation of electron depletion layer in the surface region of sensing medium [47,48]. Upon exposure to *p*-xylene, the gas molecules react with surface-bound oxygen ions, releasing electrons back to the conduction band and decreasing the thickness of electron depletion layer, thus decreasing the resistance of the sensor as observed. The processes are summarized in the following equations.

$$O_{2(gas)} \rightarrow O_{2(ads)} \quad (2)$$

$$O_{2(ads)} + e^- \rightarrow O^-_{2(ads)} \quad (3)$$

$$O^-_{2(ads)} + e^- \rightarrow 2O^-_{(ads)} \quad (4)$$

$$C_8H_{10(gas)} + 21O^-_{(ads)} \rightarrow 8CO_{2(gas)} + 5H_2O_{(gas)} + 21e^- \quad (5)$$

Sensor performance enhancement is often attributed to a synergy of factors, with gas adsorption capacity playing a key role, influenced by surface defects, surface area, and porosity. Fig. 4a shows a distinct EPR signal at 3514.5 Gauss (*g*-factor of 2.0035), indicating the presence of oxygen vacancies and unpaired electrons [49]. EPR comparison between pure $In_2O_3$ and 2 % Pt NPs-$In_2O_3$ samples reveals oxygen vacancies, with the latter exhibiting a stronger signal, suggesting a higher concentration of defects [34,50]. These defects augment active sites for gas adsorption, facilitating the reactions in Eqs. 2–4 [51]. The EIS analysis assesses the impact of Pt NPs sensitization on charge transfer resistance (Fig. 4b). In the high-frequency diffusion region, the semi-circle radius of the 2 % Pt NPs-$In_2O_3$ sample is noticeably smaller than that of the pure $In_2O_3$ sample. These results indicate that the charge transfer resistance is lower in the 2 % Pt NPs-$In_2O_3$ sample, suggesting that the incorporation of Pt NPs facilitates electron transfer at the interface. Additionally, the differential charge density and corresponding Bader charge of *p*-xylene gas molecules adsorbed on pure $In_2O_3$ and 2 % Pt NPs-$In_2O_3$ were investigated through DFT calculations (Fig. 4c). The adsorption structure model of *p*-xylene clearly shows a higher concentration of electrons transferred to the near-surface region of 2 % Pt NPs-$In_2O_3$. These results demonstrate that the introduction of Pt NPs further accelerates electron transfer, which enhances gas sensing performance.

*In situ* DRIFTS spectroscopy was employed to track chemical changes during *p*-xylene oxidation, elucidating the gas-solid reaction dynamics. In Fig. 4d, the two bands at 1564 and 1425 $cm^{-1}$ can be attributed to the in-plane skeletal vibration of the benzene ring [52]. The band at 1358 $cm^{-1}$ is ascribed to the symmetric bending vibration of the methyl group [53]. The band at 929 $cm^{-1}$ to 835 $cm^{-1}$ region belongs to the out-plane bending vibration of C–H on the para substituted benzene ring. These bands are the characteristic signals of *p*-xylene molecules [53,54]. The band at 1070 $cm^{-1}$ to 1045 $cm^{-1}$ region, which is due to the stretching vibration of C–O-C in anhydride species, indicating the formation anhydride species during the oxidation of *p*-xylene [54,55]. The spectral band at 960 $cm^{-1}$ is associated with the out-of-plane bending vibration of O–H groups in carboxylic acid species. A distinct enhancement in peak intensity is observed for the 2 % Pt NPs-$In_2O_3$ composite at this wavelength, which is markedly superior to that of the pure $In_2O_3$. This enhancement suggests a more pronounced gas-sensing reaction for the 2 % Pt NPs-$In_2O_3$ material compared to the pure $In_2O_3$. According to the experimental results and previous reports, the oxidation process of *p*-xylene can be sequentially divided into four steps and produces the corresponding intermedi-

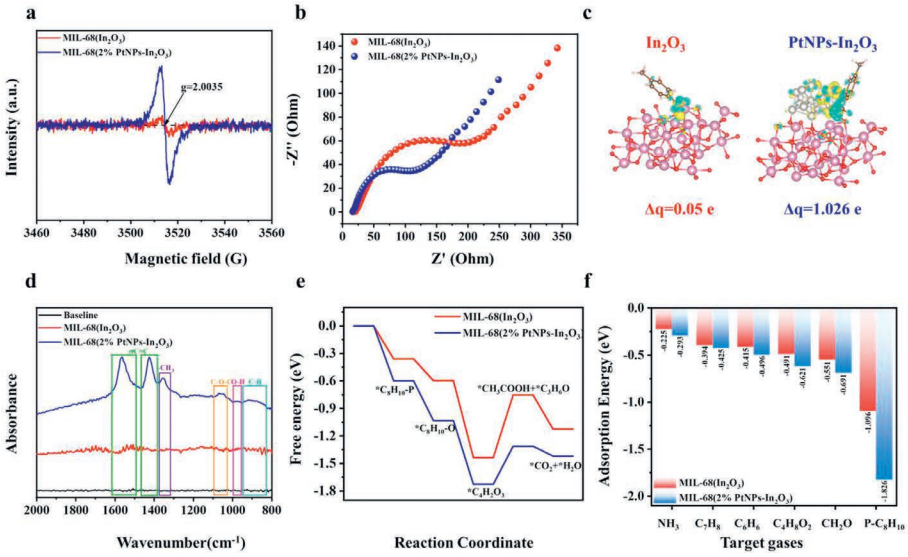



**Fig. 4.** (a) EPR spectra of the pure $In_2O_3$ and 2% Pt NPs-$In_2O_3$. (b) EIS spectrums of the pure $In_2O_3$ and 2% Pt NPs-$In_2O_3$. (c) The differential charge density and corresponding Bader charge ($\Delta Q$) of *p*-xylene gas molecules adsorbed on pure $In_2O_3$ and 2% Pt NPs-$In_2O_3$. (d) *In-situ* DRIFTS spectra of pure $In_2O_3$ and 2% Pt NPs-$In_2O_3$ exposed to 1 ppm *p*-xylene at 200 °C. (e) Energy paths of intermediates during oxidation of *p*-xylene to carbon dioxide and water vapor on pure $In_2O_3$ and 2% Pt NPs-$In_2O_3$. (f) The adsorption energies of diverse target gases on pure $In_2O_3$ and 2% Pt NPs-$In_2O_3$.

ate products, including *o*-xylene, maleic anhydride, acetic acid and acetone [52,55,56]. The process is summarized in the following expression.

$$*C_8H_{10}{-}P \rightarrow *C_8H_{10}{-}O \rightarrow *C_4H_2O_3 \rightarrow *CH_3COOH + *C_3H_6O \rightarrow *CO_2 + *H_2O \quad (6)$$

Based on the above reaction process, the Gibbs free energy of each step during the oxidation of *p*-xylene was calculated (Fig. 4e). It is worth noting that throughout the entire oxidation process, except for the third step, all other steps are exothermic and occur spontaneously which indicates that the rate of overall reaction on both pure $In_2O_3$ surface and 2% Pt NPs-$In_2O_3$ surface is mainly determined by the third step ($*C_4H_2O_3 \rightarrow *CH_3COOH + *C_3H_6O$) [57,58]. Fig. 4f compares the adsorption energy of *p*-xylene on pure $In_2O_3$ and 2% Pt NPs-$In_2O_3$, both of which are significantly lower than that of other interfering gases. Notably, the adsorption energy of *p*-xylene on 2% Pt NPs-$In_2O_3$ is −1.826 eV, much lower than the −1.096 eV observed on pure $In_2O_3$. These results highlight that 2% Pt NPs-$In_2O_3$ offers enhanced response and selectivity for *p*-xylene, due to its lower adsorption energy and stronger adsorption capacity.

Prolonged exposure to high temperatures and humidity will degrade sensor performance, affecting stability and response. In this study, a 20-day laboratory aging test was conducted to examine the impact of thermal aging on film morphology and structure. The MIL-68 (2% Pt NPs-$In_2O_3$) sensor films were aged under three conditions: 200 °C/0% RH, 200 °C/50% RH, 250 °C/0% RH to evaluate environmental effects. Additionally, *in-situ* characterization provided deeper insights into the mechanisms driving gas-sensing degradation. As indicated by the SEM characterization of the thin films (Figs. S5-S8 in Supporting information), the unaged film exhibited a smooth surface with abundant micropores (1–1.2 μm) and embedded nanoscale particles. After 20 days of aging at 200 °C/0% RH, cracks appeared, pore density decreased, and pore sizes shrank to 500–600 nm. Higher temperatures (250 °C/0% RH) further exacerbated cracking. In contrast, aging under humid conditions (200 °C/50% RH) mitigated crack formation and increased pore density, likely due to higher specific heat capacity of water, which helped alleviate thermal stress. AFM analysis further confirmed these morphological changes (Fig. S9 in Supporting information), showing an increase in surface roughness. The root-mean-square (RMS) roughness rose from 52.0006 nm (unaged) to 62.2976 nm after aging at 200 °C/0% RH, with further growth at 250 °C/0% RH (85.9525 nm). Under humid conditions (200 °C/50% RH), roughness increased to a lesser extent (69.2326 nm). While a higher surface roughness may facilitate gas adsorption, it also impedes desorption, ultimately contributing to the deterioration of sensor performance over time.

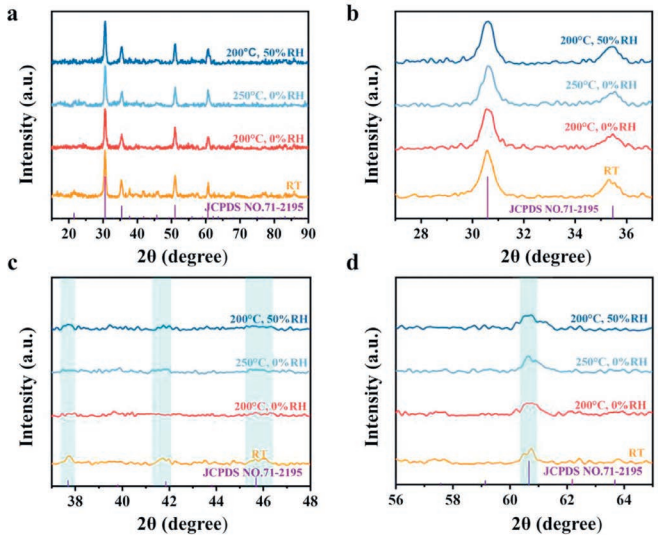



**Fig. 5.** XRD of the MIL-68 (2% PtNPs-$In_2O_3$) sensor films before and after aging under different conditions in various ranges: (a) 15°–90°; (b) 27°–37°; (c) 37°–48°; (d) 56°–65°.

XRD patterns confirmed the structural stability of MIL-68(2% PtNPs-$In_2O_3$) during aging (Fig. 5). No significant shifts in diffraction peaks were observed, indicating no phase transformation or impurity formation. Grain growth was evident, with grain sizes increasing from 9.1 nm (unaged) to 12.1–12.3 nm under various aging conditions. A decrease in crystallinity was noted, as evidenced by reduced peak intensities at 30.6°, 35.3°, 37.7°, 41.7°, and 45.7°.

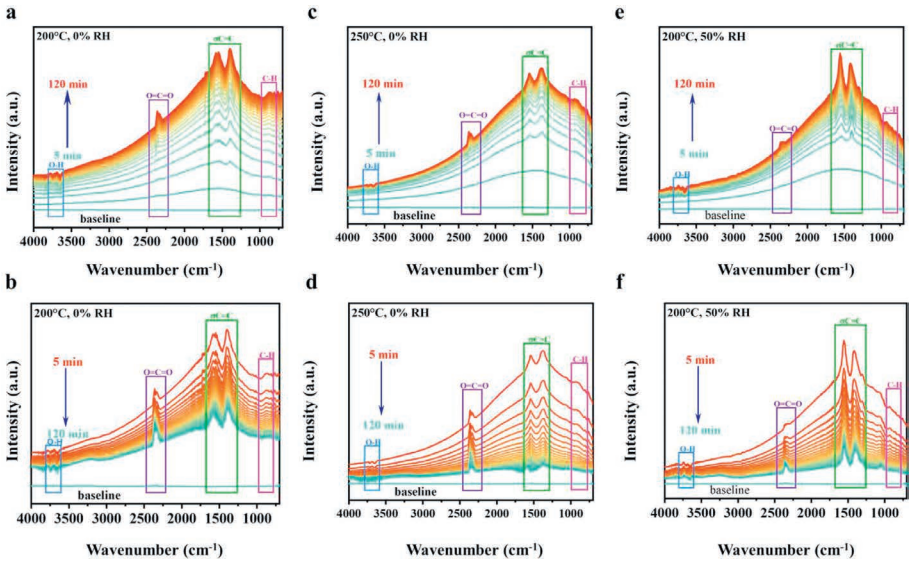



**Fig. 6.** *In-situ* DRIFTS spectra of the response and recovery processes of the MIL-68 (2 % Pt NPs-$In_2O_3$) sensor exposed to 25 ppm *p*-xylene gas under various aging conditions: At 200 °C/0 % RH, (a) response process, (b) recovery process; at 250 °C/0 % RH, (c) response process, (d) recovery process; at 200 °C/50 % RH, (e) response process, (f) recovery process.

Peak broadening at 60.7° suggested residual stress-induced lattice distortion and point defects.

To investigate the physicochemical processes occurring on the sensor surface during aging process, *in situ* DRIFTS spectroscopy was employed to monitor changes in chemical bonds and functional groups under different aging conditions. To accelerate the reaction rate and enhance the intensity of the observed phenomena, the test gas concentration was increased. Specifically, 25 ppm of *p*-xylene was continuously introduced for 2 h to observe the reaction process, followed by a 2-h exposure to air to examine the recovery behavior. As illustrated in Figs. 6a and b, characteristic vibrational bands emerged at 1549 $cm^{-1}$ and 1402 $cm^{-1}$, corresponding to in-plane skeletal vibrations of the benzene ring, while the broad absorption spanning 934–804 $cm^{-1}$ was attributed to out-of-plane bending modes of adjacent C–H bonds in the *para*-substituted benzene ring. The progressive intensification of these peaks during gas exposure (Fig. 6a) confirmed cumulative *p*-xylene adsorption on the sensor surface. Concurrently, dual peaks at 2358 $cm^{-1}$ and 2331 $cm^{-1}$ (O=C=O asymmetric stretching in $CO_2$) and a broadband at 3774–3623 $cm^{-1}$ (free O–H stretching in $H_2O$) indicated sustained redox reactions, with reaction products ($CO_2$ and $H_2O$) accumulating over time. Notably, during the air purge (Fig. 6b), incomplete recovery of absorption intensity to baseline levels after 2 h revealed irreversible surface modifications, termed “chemical poisoning”. This phenomenon likely arises from strong chemisorption of intermediates (*e.g.*, carboxylates or quinones) that block active oxygen adsorption sites, thereby impairing sensor regeneration.

At 250 °C, the absorption peak intensity related to gas adsorption is lower than at the optimal working temperature, indicating that excessively high temperatures hinder gas adsorption and reaction processes (Fig. 6c). During the recovery process (Fig. 6d), the absorption peak intensity of surface functional groups on the sensor nearly returns to baseline within 2 h, suggesting a significant reduction in the sensor's "poisoning" effect at high temperatures. The absorption bands at 1558 $cm^{-1}$ and 1417 $cm^{-1}$, 931–808 $cm^{-1}$, 2358 $cm^{-1}$ and 2329 $cm^{-1}$, as well as 3783–3617 $cm^{-1}$, correspond to the vibrations of the benzene ring skeleton, the adjacent C–H bonds in *para*-substituted benzene, the O=C=O bond in $CO_2$, and free O–H groups, respectively (Fig. 6e). The absorption peaks associated with *p*-xylene in a humid environment exhibit similar intensities to those in a dry environment, indicating that humidity does not affect *p*-xylene gas molecule-adsorption. However, $CO_2$-related absorption peaks are noticeably weaker in the humid environment, suggesting reduced redox reaction activity due to moisture interference. This points to water molecules preferentially occupying oxygen ion adsorption sites, thereby inhibiting redox processes. Similarly, in the recovery process (Fig. 6f), under humid conditions, the lower extent of reaction leads to a higher recovery level compared to a dry atmosphere; however, it still falls short of the recovery observed in high-temperature environments.

In this study, a highly sensitive *p*-xylene sensor based on Pt nanoparticle (NP)-decorated $In_2O_3$ hollow microtubes was successfully synthesized *via* a MOF-templated strategy. The 2 % Pt NPs-$In_2O_3$ sensor achieves remarkable response of 68.7 to 50 ppb *p*-xylene with an ultra-low detection limit of 10 ppb, along with excellent selectivity and long-term stability. The superior sensing performance is attributed to the synergistic effects between Pt NPs and $In_2O_3$ microtubes, as revealed by *in-situ* characterization and DFT calculations. The well-engineered Pt/$In_2O_3$ interface effectively promotes surface defect formation, enhances electron transfer, and facilitates redox reactions at the gas-solid interface, collectively contributing to the enhanced sensing properties. Furthermore, this study utilized *in-situ* characterization techniques, including SEM, XRD, AFM, and DRIFTS, to investigate the morphological evolution of the sensor film before and after aging under different conditions. Overall, this study offers a promising strategy for the development of highly sensitive ppb-level *p*-xylene gas sensors which show significant potential as a candidate for indoor monitoring of *p*-xylene pollutants. In addition, the study on the aging mechanism in this work offers valuable guidance for enhancing the long-term stability and reliability of Pt-modified $In_2O_3$ gas sensors.

## Declaration of competing interest

The authors declare that they have no known competing financial interests or personal relationships that could have appeared to influence the work reported in this paper.

## CRediT authorship contribution statement

**Huanhuan Zhang:** Writing – original draft, Investigation, Formal analysis, Data curation, Conceptualization. **Shisong Guo:** Writing – original draft, Investigation, Formal analysis, Data curation,

Conceptualization. **Yanxiang Chen:** Writing – original draft, Investigation, Formal analysis, Data curation, Conceptualization. **Yan Bai:** Writing – review & editing, Methodology, Investigation. **Shuyang Ye:** Writing – review & editing, Methodology, Investigation. **Sha Zhang:** Methodology, Investigation, Formal analysis. **Xinyi Chen:** Methodology, Investigation. **Peng Wang:** Methodology, Investigation. **Anqi Li:** Methodology, Investigation. **Long Li:** Methodology, Data curation. **Bingbing Chen:** Methodology, Data curation. **Hua-Yao Li:** Writing – review & editing, Supervision, Methodology. **Huan Liu:** Writing – review & editing, Supervision, Formal analysis.

## Acknowledgments

The authors are grateful to the financial support from National Natural Science Foundation of China (Nos. 61922032, 62271222), Science, Technology and Innovation Commission of Shenzhen Municipality (No. JCYJ20240813153442055) and Taihu Lake Innovation Fund for Future Technology (HUST: No 2024-B-9).

## Supplementary materials

Supplementary material associated with this article can be found, in the online version, at doi:10.1016/j.cclet.2025.111328.

## References

[1] A. Mirzaei, S.G. Leonardi, G. Neri, Ceram. Int. 42 (2016) 15119–15141.
[2] A.K. Pathak, C. Viphavakit, Sens. Actuator. A: Phys. 338 (2022) 113455.
[3] L.K. Sahu, D. Pal, R. Yadav, et al., Aerosol. Air Qual. Res. 16 (2016) 2405–2420.
[4] R.A. John, A.R. Kumar, Inorg. Chem. Commun. 133 (2021) 108893.
[5] M.X. Zhang, Z.H. Zhao, B. Hui, et al., J. Hazardous Mater. 416 (2021) 126161.
[6] V.D. Martins, M.A. Granato, A.E. Rodrigues, J. Chem. Engin. Data 59 (2014) 1499–1506.
[7] Y.J. Sun, Z.T. Zhao, K. Suematsu, et al., Sens. Actuator. B: Chem. 360 (2022) 131631.
[8] S.W. Park, S.Y. Jeong, J.W. Yoon, et al., ACS Appl. Mater. Interfaces 12 (2020) 51607–51615.
[9] H. Zhang, S.S. Guo, W.J. Zheng, et al., Chem. Eng. J. 469 (2023) 143927.
[10] F. Li, S.J. Guo, J.L. Shen, et al., Sens. Actuator. B: Chem. 238 (2017) 364–373.
[11] S.M. Lee, Y.K. Moon, K. Lim, et al., Sens. Actuator. B: Chem. 382 (2023) 133494.
[12] J.W. Hu, Y.D. Zou, Y. Deng, et al., Progress Mater. Sci. 150 (2025) 101409.
[13] Z.G. Pan, D.J. Wang, D.N. Zhang, et al., Sens. Actuator. B: Chem. 405 (2024) 135378.
[14] W.T. Koo, J.H. Cha, J.W. Jung, et al., Adv. Funct. Mater. 28 (2018) 1802575.
[15] B.X. Feng, Z.Z. Wang, Y.Y. Feng, et al., ACS Nano 18 (2024) 22888–22900.
[16] K. Chen, Y. Zhou, B.Y. Wang, et al., Sens. Actuator. B: Chem. 396 (2023) 134570.
[17] M. Kim, S. Park, J. Ahn, et al., ACS Sens. 9 (2024) 6492–6501.
[18] Y. Wang, G.L. Fan, S.B. Wang, et al., Adv. Mater. 34 (2022) 2204865.
[19] G. Wang, S.J. Yang, L. Cao, et al., Coord. Chem. Rev. 445 (2021) 214086.
[20] M.S. Yao, W.H. Li, G. Xu, Coord. Chem. Rev. 426 (2021) 213479.
[21] Y. Hu, B. Lin, P. He, et al., Chem. Eur. J. 21 (2015) 18739–18748.
[22] Y. Sun, Z. Dong, D. Zhang, et al., Sens. Actuator. B: Chem. 326 (2021) 128791.
[23] X.H. Liu, H. Wang, X.F. Li, et al., Sens. Actuator. B: Chem. 345 (2021) 130424.
[24] Y.J. Sun, B.L. Wang, Z.Y. Lu, et al., Sens. Actuator. B: Chem. 386 (2023) 133747.
[25] F.L. Jiang, Y. Deng, K.Y. Chen, et al., Adv. Mater. 36 (2024) 2313547.
[26] A.V. Agrawal, N. Kumar, M. Kumar, Nano-Micro Lett. 13 (2021) 38.
[27] F.D. Qu, W.A. Shang, D.T. Wang, et al., ACS Appl. Mater. Interfaces 10 (2018) 15314–15321.
[28] L.N. Jin, Q. Liu, W.Y. Sun, CrystEngComm 15 (2013) 4779–4784.
[29] U. Holzwarth, N. Gibson, Nat. Nanotechnol. 6 (2011) 534 -534.
[30] H.J. Han, G.R. Lee, Y.J. Xie, et al., Sci. Adv. 7 (2021) eabh2012.
[31] J. Schroers, Adv. Mater. 22 (2010) 1566–1597.
[32] G. Neri, A. Bonavita, G. Micali, et al., Sens. Actuator. B: Chem. 130 (2008) 222–230.
[33] S.Q. Li, Y.J. Diao, Z.J. Yang, et al., Sens. Actuator. B: Chem. 276 (2018) 526–533.
[34] P. Wang, S.S. Guo, Z.X. Hu, et al., Chem. Eng. J. 456 (2023) 140988.
[35] W.W. Sun, Y.J. Li, Y.M. Liu, et al., J. Mater. Chem. A 6 (2018) 14155–14161.
[36] Y.S. Liu, X.P. Liu, Y.B. Wang, et al., Ceram. Int. 45 (2019) 9820–9828.
[37] A.B. Chen, W.P. Zhang, X.Y. Li, et al., Catal. Lett. 119 (2007) 159–164.
[38] Q. Wang, H.C. Wu, Y.R. Wang, et al., J. Hazard. Mater. 412 (2021) 125175.
[39] B. Liu, K. Li, Y.Y. Luo, et al., Chem. Eng. J. 420 (2021) 129881.
[40] W. Liu, Y.L. Xie, T.X. Chen, et al., Sens. Actuator. B: Chem. 298 (2019) 126871.
[41] Y.K. Moon, S.Y. Jeong, Y.C. Kang, et al., ACS Appl. Mater. Interfaces 11 (2019) 32169–32177.
[42] H. Liu, M. Li, O. Voznyy, et al., Adv. Mater. 26 (2014) 2718–2724.
[43] S.S. Guo, W.B. Long, Z.X. Hu, et al., IEEE Sens. J 23 (2023) 22651–22659.
[44] Z.M. Yang, D.Z. Zhang, H.N. Chen, Sens. Actuator. B: Chem. 300 (2019) 127037.
[45] Q.Y. Duan, W.J. Zhang, L. Li, et al., Chem. Eng. J. 479 (2024) 147748.
[46] H. Wang, Y.Y. Luo, K. Li, et al., Chem. Eng. J. 427 (2022) 131631.
[47] Y.S. Xu, W. Zheng, X.H. Liu, et al., Mater. Horiz. 7 (2020) 1519–1527.
[48] P. Wang, S.S. Guo, Y.N. Zhao, et al., Sens. Actuator. B: Chem. 398 (2024) 134710.
[49] X.Y. Yang, Y.T. Shi, K.F. Xie, et al., Angew. Chem. Int. Ed. 61 (2022) e202207816.
[50] H.Y. Yuan, S.A.A.A. Aljneibi, J.R. Yuan, et al., Adv. Mater. 31 (2019) 1807161.
[51] X.Y. Yang, Y. Deng, H.T. Yang, et al., Adv. Sci. 10 (2023) 2204810.
[52] Z.W. Wang, P.J. Ma, K. Zheng, et al., Appl. Catal. B: Environ. 274 (2020) 118963.
[53] Z.B. Rui, M.N. Tang, W. Ji, et al., Catal. Today 297 (2017) 159–166.
[54] L. Li, C.B. Zhang, H. He, et al., Catal. Today 126 (2007) 338–344.
[55] T.Y. Shou, N. Xu, Y.H. Li, et al., Plasma Chem. Plasma Process. 39 (2019) 863–876.
[56] S.Y. Huang, C.B. Zhang, H. He, Catal. Today 139 (2008) 15–23.
[57] P. Wang, S. Guo, Z. Hu, et al., Adv. Sci. 10 (2023) 2302778.
[58] B. Liu, R. Feng, M. Busch, et al., ACS Nano 16 (2022) 14121–14133.